Repetitive Hole-Mask Colloidal Lithography for the Fabrication of Large-Area Low-Cost Plasmonic Multishape Single-Layer Metasurfaces

Jun Zhao, Sarah Jaber, Paul Mulvaney, Paul V. Braun, and Harald Giessen**

A novel fabrication method, multiple repetitions of hole-mask colloidal nanolithography, is introduced to create single-layer metasurfaces with complex, multishape plasmonic nanostructures that exhibit desired optical functionalities. Large-area and low-cost fabrication of different samples with independently tunable resonances are demonstrated. These single-layer metasurfaces may find applications as multiline surface-enhanced infrared absorption and broadband substrates. This fabrication method is particularly suited for the creation of large-area, single-layer C_3-rotationally symmetric, 3D chiral metasurfaces, and this approach circumvents common problems with elliptical birefringence and can be utilized for interaction with chiral substances.

1. Introduction

Nanostructuring for tailored optical functionality suffers from a lack of methods for large-area and low-cost fabrication. While electron beam lithography allows different complex shapes to be deposited onto the same substrate layer, the writing process is sequential and the fabrication is very expensive. Large-area methods, such as nanosphere lithography,[1] colloidal lithography using shadow-angle evaporation,[2] as well as hole-mask colloidal lithography[3] all enable the creation of complex plasmonic structures. These methods have already permitted the manufacture of Fano resonant sensors,[4] nanoantennas for enhanced detection of infrared (IR) vibrations,[5] nanoplasmonic hydrogen sensing,[6–8] and 3D plasmonic nanostructures.[9,10] Also, they have been used for the creation of nanodimer color routers,[11] metamaterial nanosandwiches,[12] combining various feature sizes on one surface,[13] and multielement antennas.[14,15] Other methods, such as interference lithography,[16] generate mostly simple structures, such as lines or dots. Importantly, using the abovementioned fabrication methods, only one single shaped element can be deposited, which can be repeated either regularly or in a random fashion over a very large area. No C_3- or C_4-rotationally symmetric arrangements of a single pattern can be achieved, as is required for chiral substrates. However, more flexible combinations of different complex shapes on one single metasurface are required to attain the desired tailored optical functionality, which is important in the context of chiral plasmonics,[17–23] plasmonic nanoantennas,[24,25] and materials for active plasmonics.[26,27]

To combine all the elements for the creation of low-cost highly functional nanooptical devices over square centimeter areas, we need to be able to create a wide variety of nanostructures on the same substrate with maximum flexibility, both in terms of choice of motif and choice of materials. Particularly, all elements should be mixed and placed on a single metasurface, which is on the top surface of one sample, to obtain desired plasmonic resonances in the visible and simultaneously in the infrared, and to enable interaction with other materials. This is specifically important for surface-enhanced infrared absorption (SEIRA) or surface-enhanced Raman spectroscopy (SERS). In order to fabricate truly chiral plasmonic substrates, two conditions need to be fulfilled, namely, the individual nanostructures need to exhibit chirality of a certain handedness, and the orientation of the individual chiral nanostructures needs to have C_3- or C_4-symmetry, on a single surface. If we chose to stack three different surfaces, we would not be able to obtain a single metasurface, for example, for chiral sensing. Also, for sensing applications, a single surface with resonances in the visible and in the infrared is needed to accommodate visible as well as infrared resonances for the same sensing surface. Furthermore, for samples with plasmonic parity-time (PT) asymmetry in the visible or near-IR region that consist of different materials (having the same resonance wavelength but different absorption coefficients), also a single metasurface is required.

Here, we use multiple repetitions of low-cost and high resolution hole-mask colloidal lithography to fabricate large-area high-density complex plasmonic nanostructures with variable shapes, which are mixed well and arranged on one single metasurface, for realization of real multifunctional optical devices.

J. Zhao, Prof. H. Giessen
4. Physics Institute and Research Center SCoPE
University of Stuttgart
Pfaffenwaldring 57, 70569 Stuttgart, Germany
E-mail: j.zhao@physik.uni-stuttgart.de;
h.giessen@pi4.uni-stuttgart.de
S. Jaber, Prof. P. Mulvaney
School of Chemistry and Bio21 Institute
University of Melbourne
30 Flemington Road, Victoria 3010, Australia
Prof. P. V. Braun
Department of Materials Science and Engineering
University of Illinois at Urbana-Champaign
1304 W. Green Street, Urbana, IL 61801, USA

DOI: 10.1002/adom.201400561

This method is not a simple repetition of the normal hole-mask colloidal lithography, which was used for our previous work, but an obvious advance and perfection of this fabrication technique, as more parameters must be optimized for successful fabrication of multishape metasurfaces. For example, by controlling the mask-hole density as well as the evaporation parameter, the concentration of each set of structures can be tuned, to avoid overlapping and clustering, and the size of each element can be controlled precisely. This advanced fabrication method allows for the integration of different shapes and even different materials into one nanostructured composite. To demonstrate the versatility of this approach, we combine two different sized, 90° rotated split-ring-resonators (SRRs), resulting in multiline spectra with independently tunable resonances, which could find use in multiline enhanced SEIRA. As a second example, we prepare three different SRRs with various arc lengths on one single metasurface using three repetitions of hole-mask lithography for broadband spectra. Finally, we combine multishape deposition and 3D fabrication to create large-area, C_3-symmetric chiral metasurfaces,[28–30] which exhibit optical circular dichroism (CD).[31–33]

2. Fabrication Processes of Repetitive Hole-Mask Colloidal Lithography

The repetitive hole-mask fabrication process is depicted in **Figure 1**. We use conventional hole-mask colloidal lithography[4,5,17] to create the first set of structures. The mask preparation includes spin coating of a poly(methyl methacrylate) (PMMA) layer (Figure 1a), drop casting of positively charged polyelectrolyte solution poly(diallyldimethylammonium chloride) (PDDA) (Figure 1b), followed by drop casting of a negatively charged polystyrene (PS) spheres (Figure 1c), evaporation of a 20 nm gold film as an etching mask (Figure 1d), lift-off of the PS spheres (Figure 1e), and finally oxygen plasma etching (Figure 1f). Afterward, we use tilted-angle-rotation evaporation[34] with the prepared hole-mask to create a set of SRRs (Figure 1g). The second set of structures is formed by repeating the same hole-mask preparation process on the sample coated with the first set of gold structures. A slight waviness of the second PMMA layer arises from modulation by the first set of structures. Hence, the distribution of the positive charge from the PDDA solution is strongly influenced. More positive charge accumulates on the regions where there are no metallic structures under the PMMA film (Figure 1h). The PS spheres of the second repetition, which define the positions of the mask-holes, prefer to settle on these metal-free regions through electrostatic interactions. Utilizing the second gold hole-mask, another set of nanostructures with a different geometry to the first set can be evaporated over empty regions of the substrate (Figure 1i). By optimizing the density of the PS spheres, and by choosing an appropriate design for the nanostructures being deposited, the two different structures can be well separated laterally. By controlling the concentration of PS spheres deposited for each repetition, multishape samples with up to three different types of nano-motifs incorporated into the final material are formed, as shown in Figure 1j,k. Of course, as the number of different shapes increases, the fabrication becomes more difficult and the overall optical quality of the sample slightly decreases.

2.1. Control of the Mask-Hole Density

The most important parameter for repetitive hole-mask fabrication is the number of deposited PS spheres used in each fabrication cycle. To enable a larger number of different structures mixed on the same substrate, the concentration of the PS sphere solution should be tuned to a suitably low value to avoid clustering after structure deposition and to achieve enough strong signal-to-noise ratio for the later optical measurement. The concentration of the PDDA solution should also be appropriate to the PS solution concentration due to electrostatic interactions. The details of the mask-hole density controlling were discussed in ref. [15]. In this paper, we use 0.005 wt% PS solution for two-shape samples and 0.002 wt% PS solution for three-shape samples. The PDDA solution used for preparing both types of samples is 0.1 wt%. In our case, the neighbor-to-neighbor distance of the fabricated structures is larger than a few tens of nanometers, hence plasmon hybridization effects due to lateral coupling are unlikely to play an important role.[35]

2.2. Control of the Tilted Evaporation Angle

Another important parameter for the repetitive fabrication process is the tilted angle θ for the evaporation. For ring-like structure geometry, the radius of the ring r depends on the PMMA layer thickness h_0 and the tilted angle θ with $r = h_0 \tan\theta$.[5] For the second fabrication cycle, the spin-coated PMMA layer on a substrate, which already has nanostructures on it, is slightly thicker than the PMMA spin-coated initially on a clean substrate, even using the same spin coating parameters. Due to the existence of the first set nanostructures on the substrate, the hydrophobicity of the substrate surface is enhanced, resulting in a thicker spin coated PMMA layer. **Figure 2**a,b show scanning electron microscope (SEM) images of two-shape samples, which are fabricated by two repetitions of mask preparation and subsequence metal evaporation. We use exactly the same tilt angle $\theta = 25°$ for the two-SRR sample and $\theta = 23°$ for the two-3D SRR sample, but the size of each set of structures is definitely different. The second set of ring structures, which are evaporated in the second fabrication cycle, show a larger radius r than that of the first set, due to a larger thickness h_0 of the second time spin coated PMMA layer. In order to obtain the same structure size for the first and second fabrication cycle, we introduce a correction factor $\Delta\theta = -1.5°$, as shown in Figure 2c. The 3D SRR structures fabricated in the second cycle using a tilted evaporation angle $\theta_{2nd} = 19–1.5° = 17.5°$ show the same size as the structures fabricated in the first cycle with $\theta_{1st} = 19°$. For the third fabrication cycle, we use the same parameters as in the second cycle, which means there is nearly no difference in the PMMA layer thickness which is spin coated on the samples with one and two set fabricated nanostructures on them. The very slightly increased concentration of the nanostructures on the substrate does not affect the surface hydrophobicity of the sample. Therefore, to achieve the same

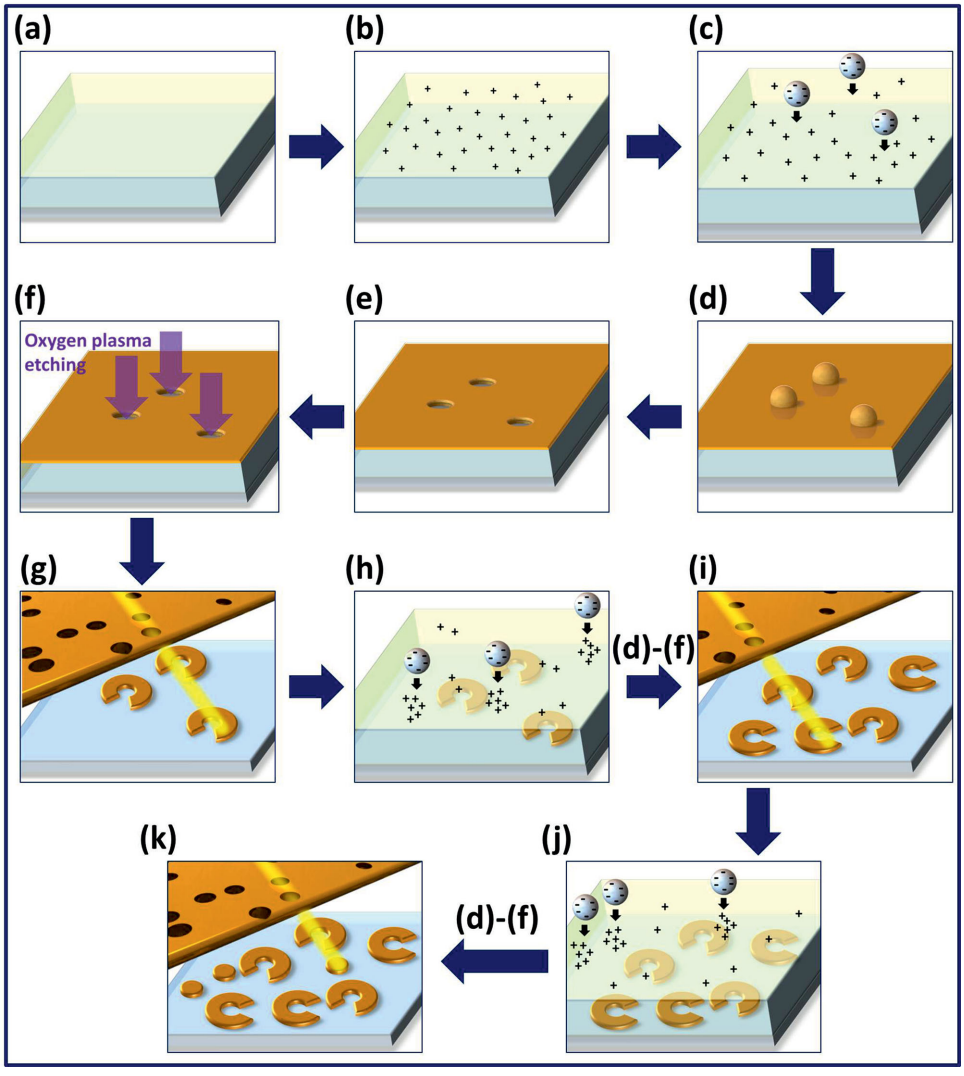

Figure 1. Fabrication scheme of repetitive hole-mask colloidal lithography. a) Spin-coating of a film of PMMA onto a substrate. b) Drop-casting of positively charged PDDA solution onto the PMMA film. c) Deposition of negatively charged PS spheres onto the PMMA film. d) Evaporation of a thin layer of gold as an etching mask onto the PS spheres. e) Removal of the PS spheres. f) Oxygen plasma etching. g) Tilted-angle-rotation evaporation of the first set of gold nanostructures (in this case SRRs) using the prepared gold hole-mask created by the first layer of PS spheres. h) Deposition of a second layer of PS spheres onto a second PMMA film, which is spin coated onto the previous sample and covered with PDDA, then repeating processes d–f). i) Evaporation of a second set of gold nanostructures (in this case 90° rotated SRRs) using the second hole-mask prepared on the same substrate. j) Deposition of a third layer of PS spheres onto a third PMMA film, then repeating of processes d–f) again. k) Evaporation of a third set of gold nanostructures (in this case plasmonic disks) using a third hole-mask on the same substrate layer. This method can in principle be repeated, until a high density of structures is reached.

structure size in each fabrication cycle, we only need to use the correction factor $\Delta\theta = -1.5°$ for the second cycle, and then for the rest of the fabrication process, the same parameters can be used as in the second cycle. Based on this, we can vary the structure size of each set elements of one single metasurface very precisely and reproducibly.

3. Optical Responses of the Fabricated Multishape Single-Layer Metasurfaces

Figure 3 shows the results of different multishape single-layer metasurfaces fabricated with repetitive hole-mask lithography. In the SEM images (shown in the first row), clearly different structure geometries mixed and together on the same substrates with well separated arrangement are observed. All samples are measured using Fourier transform infrared (FTIR) spectroscopy with 0° (black curve) and 90° (red curve) polarization (shown in the second row), as defined in the upper-right corner in Figure 3a. Finite-difference time-domain (FDTD) code (CST Microwave Studio) is used for the simulations, which are shown in the third row. The refractive index of the glass substrate is assumed to be $n = 1.5$, and a Drude model with plasma frequency $\omega_p = 1.37 \times 10^{16}$ Hz and a damping constant $\kappa = 1.2 \times 10^{14}$ Hz is used to describe the permittivity of bulk gold. The period used in the simulation is the average

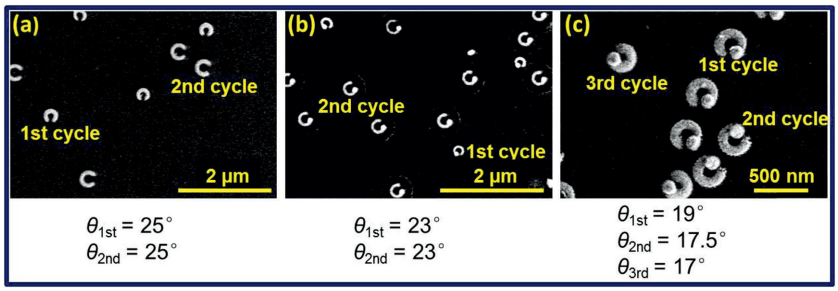

Figure 2. SEM images of the fabricated two- and three-shape samples with the tilted angles θ for each cycle evaporation. a) Two 90° rotated SRR shapes, which are evaporated using the same tilt angle $\theta = 25°$. b) Two 120° rotated 3D SRR shapes, which are evaporated with the same tilt angle $\theta = 23°$. c) C_3-symmetric 3D SRR shapes using tilt angle $\theta = 19°$ for the first time, $\theta = 17.5°$ for the second time, and $\theta = 17°$ for the third time evaporation, respectively.

distance of the neighboring structures, which depends on the coverage over the entire substrate.

The first example is a two-shape sample consisting of SRRs with two different sizes and perpendicular gap directions, as shown in Figure 2a. Multiresonance spectra can be easily achieved through this design. For 90° polarization, the first-order SRR mode of the smaller structures lies at about 2800 nm, the third-order mode at about 1200 nm, while the second-order mode of the larger structures is at around 1900 nm and these three modes are readily observed in both experimental and simulated spectra. However, for 0° polarization we only see two resonances: the first-order mode of the larger SRRs at about 3500 nm and one strong dip at around 1400 nm. This well-modulated resonance is due to the overlap of the second-order mode of the smaller SRRs and the third-order mode of the larger SRRs. This phenomenon indicates that by suitable design of multishape samples, we can also reduce the number of resonances in the multiline spectra or enhance the modulation depth of the expected resonance. Actually, a single-SRR sample already exhibits three resonances simultaneously under 45° polarization illumination, as discussed in ref. [5], but it is difficult to tune all the resonances independently. With this two-SRR design, more tunable resonances for a possible multiline resonant SEIRA measurement are obtained, which is important for detection of a large number of different vibrational modes in a single molecule or even several different molecules at the same time. This sample might be modified in the future to serve as plasmonic PT-asymmetric metasurface[36] in the visible or near-IR for the case when two different materials are used and the resonances are kept the same. Our method would constitute a very elegant and simple fashion to achieve this functionality over large areas.

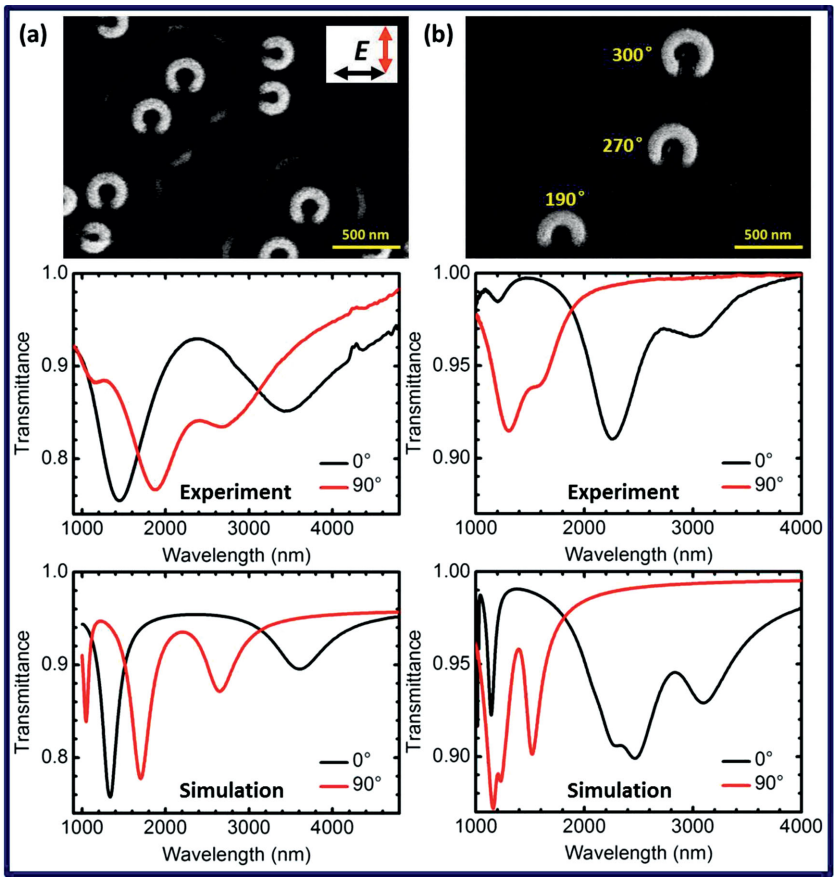

Figure 3. A variety of different multishape nanostructures fabricated by multiple repetition of hole-mask colloidal nanolithography (shown in the first row) and the corresponding optical spectra from FTIR measurements (shown in the second row) and FDTD simulations (shown in the third row). All the samples are measured with 0° (black curve) and 90° (red curve) polarization, which are defined and depicted in Figure 3a upper-right corner. a) Two different sized SRR structures with orthogonal gap directions. b) Three-repetition SRRs sample with different arc lengths.

For many applications, broadband spectra are required. Figure 3b shows one of the possible designs: a three-SRR-shape sample fabricated with three repetitions of hole-mask lithography. The three SRR geometries have the same radius and gap directions but different arc lengths, which are easily prepared by changing the evaporation parameters. The differences in the arc lengths are adjusted to ensure that the excited plasmon modes of the three SRRs are close enough to realize broadband features around 2000–3000 nm.

Our method allows for different, more flexible designs of multifunctional nanooptical devices, such as two-shape samples consisting of mixed gold SRRs and disk structures, which is a possible platform to realize simultaneous SEIRA and SERS, as the SRR structures with resonances in the infrared can be used for antenna-enhanced SEIRA[5] and the disk structures provide a plasmon resonance near the visible range for excitation with a visible Raman laser. The

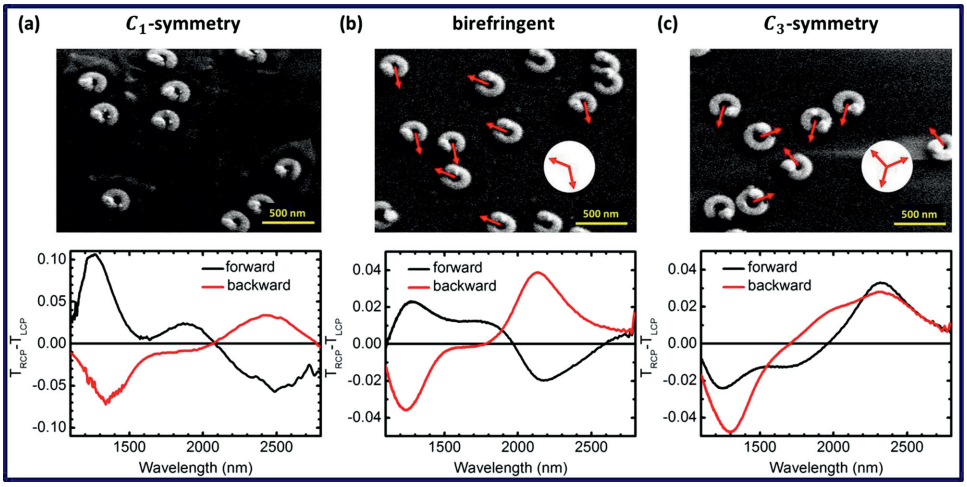

Figure 4. 3D SRRs with C_1-symmetry a), birefringent- b), and C_3-symmetry c), which are fabricated via one, two, and three repetitions of hole-mask colloidal nanolithography, respectively. The SEM images are shown in the first row, with red arrows indicating the gap directions of the 3D SRRs. All the spectra are collected with a FTIR spectrometer using left-handed and right-handed circularly polarized light in forward (black curve) and backward (red curve) directions. In the second row, we display the CD spectra of the three samples for both directions of illumination.

optical response of such a sample has been shown and discussed in ref. [17].

Particularly, for vibrational detection of various substances, it is essential to obtain infrared spectra of the entire fingerprint region, which means that several vibration bands should be plasmonically amplified. For example, ultrasensitive detection of TNT requires observation of the vibration bands at 6.45 and 7.4 μm.[37] RDX, another dangerous explosive, exhibits fingerprint vibrations at 6.3, 7.5, 8.0, and 9.7 μm.[38] Commonly, very expensive quantum cascade lasers are used for this detection, and the whole vibrational region of interest cannot be spanned by a single laser. A simple resonant antenna chip with four different antenna sizes matching their plasmonic resonances with the vibrational bands, fabricated by our novel repetitive colloidal hole lithography method, would easily create a single substrate that can be used in a cheap compact FTIR spectrometer for this standoff detection.

Using single-repetition hole-mask colloidal lithography, structures with more than one material or even with 3D geometries can also be created.[6] As shown in the SEM image in **Figure 4**a, we first evaporate magnesium fluoride (MgF_2) disks with a thickness of about 30 nm. Afterward, we change the material crucible in the vacuum chamber and directly evaporate normal gold SRRs using the same hole-mask. Using a polar angle controllable motor during the evaporation, one side of the gold SRRs is exactly deposited on the MgF_2 disks. Due to the clogging effect of the hole-mask, the fabricated disks are not perfectly shaped cylinders, but rather more circular truncated cones. Thus, one side of the gold SRRs has a small vertical slope to form a 3D geometry.

By combining this 3D fabrication and multishape fabrication as introduced before, large-area 3D SRRs, which exhibit birefringent- or even C_3-symmetry, can be realized, as shown in the SEM images of Figure 4b,c, with the red arrows pointing to different gap directions in these samples. In principle, one could also stack different twisted layers above each other.[39] However, in this case, the relative alignment plays a crucial role.[40] Additionally, stacking does not allow for interaction of the submersed layers with materials on the surface,[41] for example, in the case of refractive index sensing or SERS/SEIRA. Moreover, even though a C_1-symmetric sample shows a signal when measured in a CD spectrometer, this signal arises due to elliptical birefringence and is not true evidence for circular dichroism. Only C_3- or C_4 symmetric nanostructures will exhibit optical chirality, as discussed in ref. [42], Supporting Information. In order to demonstrate the potential of our multishape fabrication technique for creating novel optical functions in materials, we experimentally verify the optical CD of all the 3D SRR samples. Chiral structures cannot be superimposed on their mirror images,[43] and the left- or right-handed version of them can only be distinguished from their interaction with circularly polarized light, therefore we usually examine the CD spectra to characterize them. CD is defined as the absorbance difference between left- and right-handed circularly polarized light. In our experiment, the FTIR setup only allows reflectance measurements for circularly polarized light over a limited wavelength range. Within this range the absorbance spectra and 1 − Transmittance spectra are comparable,[44] hence we use $\Delta T = T_{RCP} - T_{LCP}$ to denote CD spectra in our experiment. A truly chiral structure with C_3- or C_4-symmetry, which makes the sample uniaxial in the z-direction, shows an illumination-direction (+ and −z direction) independent CD spectrum. Due to elliptical birefringence arising from the biaxiality of non-C_3- or C_4-symmetric samples, contributions from polarization conversion are expected to the measured spectra, which would change the sign of the CD spectra for different illumination directions. CD of birefringent samples can be calculated with the formula $\Delta T = 1/2(\Delta T_{forward} - \Delta T_{backward})$.[42] In consequence, we measure transmittance of all our 3D SRR samples for perpendicularly incident left- and right-handed circularly polarized light with both forward and backward light propagation, as shown in Figure 4.

Figure 4a,b show the SEM images (top) and the measured CD spectra for both illumination directions (bottom) of C_1- and birefringent symmetric right-handed 3D SRRs. The CD spectra of both samples measured with forward (black curve) and backward (red curve) illuminations exhibit nearly mirror symmetry with respect to the zero line, confirming that there is no true chirality in the C_1- and birefringent symmetric samples. The maximum transmittance differences ΔT of the C_1-symmetric sample are about 5% at around 2500 nm and 8%–10% at around 1300 nm, these values agree with the positions of the first- and the second-order SRR modes, respectively. For the birefringent symmetric sample, one maximum ΔT of about 2–4% is observed at around 2200 nm, and the other one at about 1200 nm. The spectral features of the two samples are similar because the designs of both samples are similar. The small blue shift of the CD responses of the birefringent sample stems from the relative smaller SRR-size.

As shown in Figure 4c, the CD spectra of C_3-symmetric left-handed 3D SRRs for forward and backward illumination are qualitatively similar to each other, except for broadening and some shift of the resonance due to fabrication and measurement tolerances, which can be easily improved by more accurate manufacturing in the future. However, compared to the samples in Figure 4a,b, this sample definitely exhibits the key signature of optical chirality, namely, circular dichroism, which is independent of illumination direction. This confirms both the efficacy and the quality of our multishape fabrication method.

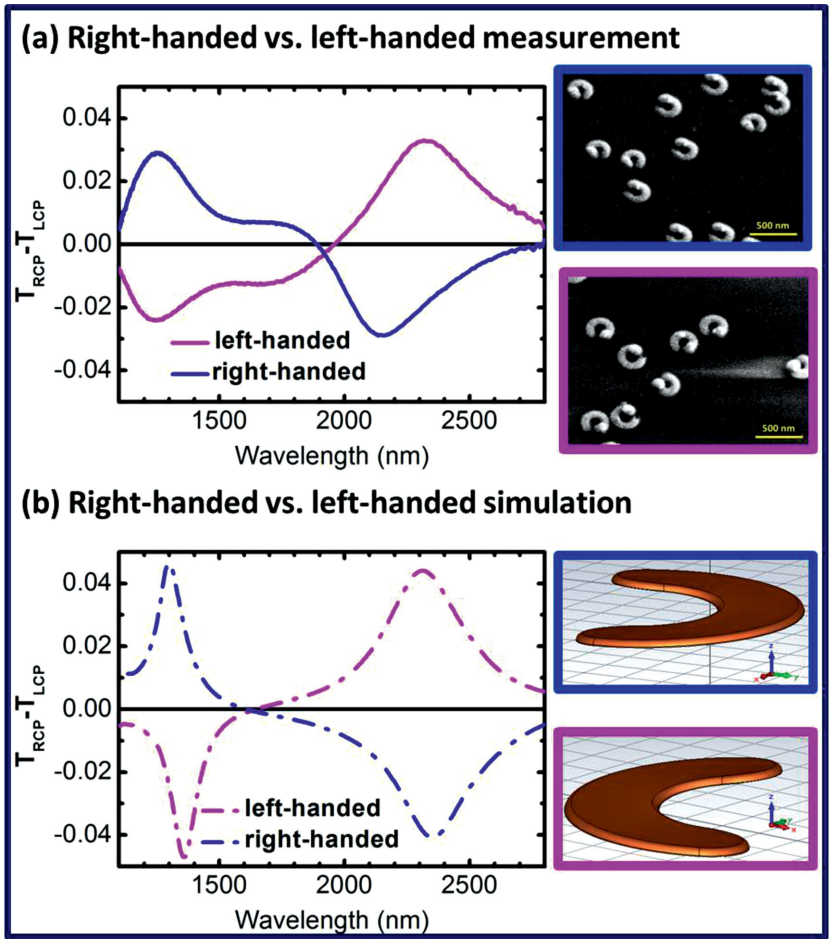

Figure 5. Comparison of the right-handed and left-handed 3D chiral SRRs. a) SEM images of the right-handed chiral SRRs (blue label) and the C_3-symmetric left-handed chiral SRRs (pink label). In the middle, we show the calculated (as described above) CD spectrum (blue curve) of the right-handed sample compared to the forward measured CD spectrum (pink curve) of the left-handed sample. b) Simulations of the right-handed (blue dashed-dotted curve) and left-handed chiral SRRs (pink red dashed-dotted curve).

To further study the chirality of the samples, we compare the CD spectra of the 3D chiral SRRs with different handednesses. **Figure 5**a shows the SEM images of the right-handed and left-handed structures together with the corresponding CD spectra (blue label and curve for right-handed version and pink for left-handed version). It is clearly recognized that they exhibit opposite chiral responses, as expected. Again, two main resonances are observed at about 1300 nm and 2300 nm. Figure 5b depicts the corresponding simulations, which agree well with our experiment. The deviations arise mainly from the fact that the exact modeling of our experimental shape is very difficult. For simplicity, a continuously sloping SRR shape is assumed, which is embedded in an average refractive index background material with $\varepsilon_{\text{avg}} = \frac{1}{2}(\varepsilon_{\text{air}} + \varepsilon_{\text{substrate}})$. This is a somewhat idealized scenario, as the real structure is a somewhat flatter SRR with one corner on the MgF_2 disk. Therefore, the theoretically predicted CD value is higher than the experimentally observed one, and the simulated resonances are much narrower without inhomogeneous broadening.

4. Conclusion

In summary, we have demonstrated that multiple repetitions of hole-mask colloidal lithography on the same substrate in combination with sparse hole-coverage and controlled tilted-angle-rotation evaporation enable multishape nanofabrication on the very same substrate layer. This method is intrinsically large-area and low-cost. Simultaneously, it allows for a large variety of structural designs, which includes 3D structures, stacking, and different materials. We have demonstrated the flexibility of our fabrication method on four different types of diverse plasmonic multishape single-layer metasurfaces with excellent optical functionality, namely, plasmonic SRRs together with disks on a single substrate layer, which enable the measurement of SEIRA and SERS on the same sample; an arrangement of differently oriented SRRs with different sizes, which would allow for multiline SEIRA measurements; a group of SRRs with different arc lengths at the same orientation, which give broadband resonant behavior; and finally C_3-rotationally symmetric 3D chiral SRRs, which show

truly chiral optical responses independent of propagation direction (–z and +z). Such chiral metasurfaces could find use as tunable waveplates in the near- and mid-infrared spectral region, as well as enhancement antennas for vibrational circular dichroism.

In the future, we will be able to combine our structures in hybrid systems to engineer unprecedented functionalities in nanoplasmonic systems. This includes nonreciprocal materials such as bismuth iron garnet (BIG), that results in plasmonically enhanced Faraday rotation[45] or the magneto-optical Kerr effect; or materials such as palladium (Pd) or yttrium (Y),[46,47] which can give rise to complex plasmonic sensors; and also phase change materials such as VO_2 or GeSbTe.[48,49] This method also constitutes a very elegant and simple approach to the fabrication of large-area plasmonic PT-asymmetric metasurfaces in the visible or near-IR for the case when two different absorbing materials are used and the resonances are kept the same.

Acknowledgements

This work was supported by DFG, BMBF, ERC (ComplexPlas), AvH-Stiftung, GIF, BW-Stiftung, and MWK-BW. P.M. acknowledges support from MPI-FKF and ARC Grant LF100100117. P.V.B. acknowledges support through the Bessel Prize from AvH and BW-Spitzenforschung II. S.J. acknowledges funding through ANN and DIISR. We acknowledge A. Tittl for the TOC illustration.

Received: November 28, 2014
Revised: December 8, 2014
Published online: January 7, 2015

[1] U. Ch. Fischer, H. P. Zingsheim, *J. Vac. Sci. Technol.* **1981**, *19*, 881.
[2] N. Vogel, J. Fischer, R. Mohammadi, M. Retsch, H. J. Butt, K. Landfester, C. K. Weiss, M. Kreiter, *Nano Lett.* **2011**, *11*, 446.
[3] H. Fredriksson, Y. Alaverdyan, A. Dmitriev, C. Langhammer, D. S. Sutherland, M. Zäch, B. Kasemo, *Adv. Mater.* **2007**, *19*, 4297.
[4] J. Zhao, C. Zhang, P. V. Braun, H. Giessen, *Adv. Mater.* **2012**, *24*, OP247.
[5] S. Cataldo, J. Zhao, F. Neubrech, B. Frank, C. Zhang, P. V. Braun, H. Giessen, *ACS Nano* **2012**, *6*, 979.
[6] C. Langhammer, I. Zoric, B. Kasemo, *Nano Lett.* **2007**, *7*, 3122.
[7] T. Shegai, P. Johansson, C. Langhammer, M. Käll, *Nano Lett.* **2012**, *12*, 2464.
[8] A. Yang, M. D. Huntington, M. F. Cardinal, S. S. Masango, R. P. Van Duyne, T. W. Odom, *ACS Nano* **2014**, *8*, 7639.
[9] B. Frank, X. Yin, M. Schäferling, J. Zhao, S. M. Hein, P. V. Braun, H. Giessen, *ACS Nano* **2013**, *7*, 6321.
[10] R. Ogier, Y. Fang, M. Svedendahl, P. Johansson, M. Käll, *ACS Photon.* **2014**, *1*, 1074.
[11] T. Shegai, S. Chen, V. D. Miljkovic, G. Zengin, P. Johansson, M. Käll, *Nat. Commun.* **2011**, *2*, 481.
[12] A. Dmitriev, T. Pakizeh, M. Käll, D. S. Sutherland, *Small* **2007**, *3*, 294.
[13] R. Esteban, R. Vogelgesang, J. Dorfmüller, A. Dmitriev, C. Rockstuhl, C. Etrich, K. Kern, *Nano Lett.* **2008**, *8*, 3155.
[14] S. Syrenova, C. Wadell, C. Langhammer, *Nano Lett.* **2014**, *14*, 2655.
[15] A. Nemiroski, M. Gonidec, J. M. Fox, P. Jean-Remy, E. Turnage, G. M. Whitesides, *ACS Nano* **2014**, *8*, 11061.
[16] J. P. Spalla, A. M. Hawryluk, D. R. Kania, *J. Vac. Sci. Technol. B* **1995**, *13*, 1973.
[17] J. Zhao, B. Frank, F. Neubrech, C. Zhang, P. V. Braun, H. Giessen, *Beilstein J. Nanotechnol.* **2014**, *5*, 577.
[18] X. Yin, M. Schäferling, B. Metzger, H. Giessen, *Nano Lett.* **2013**, *13*, 6238.
[19] A. Kuzyk, R. Schreiber, Z. Fan, G. Pardatscher, EM. Roller, A. Högele, F. C. Simmel, A. O. Govorov, T. Liedl, *Nature (London)* **2012**, *483*, 311.
[20] Z. Fan, A. O. Govorov, *Nano Lett.* **2010**, *10*, 2580.
[21] Z. Fan, A. O. Govorov, *Nano Lett.* **2012**, *12*, 3283.
[22] M. Decker, M. W. Klein, M. Wegener, S. Linden, *Opt. Lett.* **2007**, *32*, 856.
[23] J. K. Gansel, M. Thiel, M. S. Rill, M. Decker, K. Bade, V. Saile, G. von Freymann, S. Linden, M. Wegener, *Science* **2009**, *325*, 1513.
[24] M. Husnik, S. Linden, R. Diehl, J. Niegemann, K. Busch, *Phys. Rev. Lett.* **2012**, *109*, 233902.
[25] R. Filter, K. Slowik, J. Straubel, F. Lederer, C. Rockstuhl, *Opt. Lett.* **2014**, *39*, 1246.
[26] K. F. MacDonald, Z. L. Samson, M. I. Stockman, N. I. Zheludev, *Nat. Photon.* **2009**, *3*, 55.
[27] M. Ren, E. Plum, J. Xu, N. I. Zheludev, *Nat. Commun.* **2012**, *3*, 833.
[28] C. Helgert, E. Pshenay-Seyerin, M. Falkner, C. Menzel, C. Rockstuhl, E. B. Kley, A. Tünnermann, F. Lederer, T. Pertsch, *Nano Lett.* **2011**, *11*, 4400.
[29] C. Rockstuhl, C. Menzel, T. Paul, F. Lederer, *Phys. Rev. B* **2009**, *79*, 035321.
[30] C. Menzel, C. Rockstuhl, T. Paul, F. Lederer, *Appl. Phys. Lett.* **2008**, *93*, 233106.
[31] T. J. Davis, E. Hendry, *Phys. Rev. B* **2013**, *87*, 085405.
[32] F. Eftekhari, T. J. Davis, *Phys. Rev. B* **2012**, *86*, 075428.
[33] E. Hendry, R. V. Mikhaylovskiy, L. D. Barron, M. Kadodwala, T. J. Davis, *Nano Lett.* **2012**, *12*, 3640.
[34] M. C. Gwinner, E. Koroknay, L. Fu, P. Patoka, W. Kandulski, M. Giersig, H. Giessen, *Small* **2009**, *5*, 400.
[35] N. Liu, H. Giessen, *Angew. Chem.* **2010**, *49*, 9838.
[36] M. Lawrence, N. Xu, X. Zhang, L. Cong, J. Han, W. Zhang, S. Zhang, *Phys. Rev. Lett.* **2014**, *113*, 093901.
[37] M. B. Pushkarsky, I. G. Dunayevskiy, M. Prasanna, A. G. Tsekoun, R. Go, C. K. N. Patel, *Proc. Natl. Acad. Sci. USA* **2006**, *103*, 19630.
[38] M. E. Morales-Rodríguez, L. R. Senesac, S. Rajic, N. V. Lavrik, D. B. Smith, P. G. Datskos, *Opt. Lett.* **2013**, *38*, 507.
[39] Y. Zhao, M. A. Belkin, A. Alù, *Nat. Commun.* **2012**, *3*, 870.
[40] M. Hentschel, M. Schäferling, B. Metzger, H. Giessen, *Nano Lett.* **2013**, *13*, 600.
[41] M. Schäferling, X. Yin, N. Engheta, H. Giessen, *ACS Photon.* **2014**, *1*, 530.
[42] M. Hentschel, M. Schäferling, T. Weiss, N. Liu, H. Giessen, *Nano Lett.* **2012**, *12*, 2542.
[43] W. H. Thomson, L. Kelvin, *Baltimore Lecture*, C. J. Clay and Sons, London **1884**.
[44] R. Kuroda, T. Hrada, Y. Shindo, *Rev. Sci. Instrum.* **2001**, *72*, 3802.
[45] J. Y. Chin, T. Steinle, T. Wehlus, D. Dregely, T. Weiss, V. I. Belotelov, B. Stritzker, H. Giessen, *Nat. Commun.* **2013**, *4*, 1599.
[46] N. Liu, L. Tang, M. Hentschel, H. Giessen, A. P. Alivisatos, *Nat. Mater.* **2011**, *10*, 631.
[47] N. Strohfeldt, A. Tittl, M. Schäferling, F. Neubrech, U. Kreibig, R. Griessen, H. Giessen, *Nano Lett.* **2014**, *14*, 1140.
[48] K. Appavoo, D. Y. Lei, Y. Sonnefraud, B. Wang, S. T. Pantelides, S. A. Maier, R. F. Haglund, Jr., *Nano Lett.* **2012**, *12*, 780.
[49] A. K. U. Michel, D. N. Chigrin, T. W. W. Maß, K. Schönauer, M. Salinga, M. Wuttig, T. Taubner, *Nano Lett.* **2013**, *13*, 3470.